Numerical analysis of reinforced soil-retaining wall structures with cohesive and granular backfills

E. Guler[1], M. Hamderi[2] and M. M. Demirkan[3]

[1]*Professor, Department of Civil Engineering, Bogazici University, 34342, Bebek, Istanbul, Turkey, Telephone: +90 212 359 6452, Telefax: +90 212 287 2463, E-mail: eguler@boun.edu.tr*
[2]*Research Assistant, Drexel University, Department of Civil, Architecture and Environmental Engineering, Philadelphia, PA 19104, USA, Telephone: +1 215 895 2272, Telefax: +1 215 895 1363, E-mail: mh337@drexel.edu*
[3]*Former Research Assistant, Bogazici University, 34342, Bebek, Istanbul, Turkey, Telephone: +1 301 405 1618, Telefax: +1 301 405 2585, E-mail: demirkan@umd.edu*

Received 26 September 2006, revised 3 January 2007, accepted 15 September 2007

ABSTRACT: The failure mechanisms of reinforced soil segmental walls with extensible reinforcements were studied by performing a numerical analysis using the finite element method. The numerical approach was first verified against the results of three instrumented full-scale structures reported in the literature. Finite element models with different combinations of reinforcement spacing, reinforcement length and backfill soil were analysed. The $\phi-c$ reduction method, which is a special shear strength parameter reduction technique, was applied to simulate the failure conditions. The results of $\phi-c$ reduction analysis were used to evaluate assumptions used in current design procedures for geosynthetic-reinforced soil walls. In particular, shear strains were used to identify failure surfaces. Interpretation of the results indicated that, for both granular and cohesive backfills, the potential failure surface gradually shifts to a direct sliding mode as the system approaches failure. As a result, under working loads the potential failure surface used in current design analysis is correct, but the failure plane of a geosynthetic-reinforced soil-retaining wall at failure approaches a direct sliding type or a bilinear plane, which starts from the toe of the wall with a very shallow slope.

KEYWORDS: Geosynthetics, Reinforced soil, Geotextile, Failure surface, Finite element analysis, Shear strains

REFERENCE: Guler, E., Hamderi, M. & Demirkan, M. M. (2007). Numerical analysis of reinforced soil-retaining wall structures with cohesive and granular backfills. *Geosynthetics International*, **14**, No. 6, 330–345. [doi: 10.1680/gein.2007.14.6.330]

1. INTRODUCTION

Reinforced soil is a composite structure formed by the interaction of soil with metallic or polymer reinforcements. In this way, the earth mass tends to act as a cohesive monolithic body, supporting its own weight as well as the external loadings for which it has been designed (Elias and Christopher 1997). The main function of the reinforcement layers inside the soil is to improve the tensile resistance of the soil body by friction created along the reinforcement surface and passive resistance in the transverse direction to the displacement. The average shear stress carried by the soil is reduced, whereas the average normal stress is increased on the failure surface.

Although reinforced soil-retaining structures have been constructed for 35 years, their failure mechanisms are not fully understood (Leshchinsky and Vulova 2001). Understanding failure mechanisms is possible with laboratory and field tests as well as with finite element analysis, but the conventional design of segmental retaining wall structures is commonly performed by using limit equilibrium analysis. The failure planes used in current design codes reflect the findings of failure planes determined for conventional retaining structures and adapted to metallic reinforcement materials. This adaptation gradually included geosynthetic reinforcement. The objective of this study is to investigate the assumptions made in conventional design by performing a numerical analysis of failure mechanisms.

In addition, for conventional design the backfill material is automatically assumed to be a purely granular soil. However, the advantage of geosynthetic reinforcement is that it does not have a corrosion risk, so the use of clean granular soil is not necessary from a durability point of view. Especially in regions where clean granular material is difficult to obtain or expensive, the use of marginal

soils can be an advantage for geosynthetic-reinforced walls. Nevertheless, poorly draining backfills (i.e. marginal soils, cohesive soils) have been successfully used as backfill when free-draining soils were not readily available (Benjamim *et al.* 2007). Experimental studies on marginal soils have shown that these soils can be used if necessary forethought is taken (Zornberg and Mitchell 1994). In the current study the behaviour of cohesive backfill materials was also investigated.

2. PREVIOUS RESEARCH

Despite the fact that many reinforced soil walls have been safely constructed using extensible reinforcement and are performing well to date, the roles of the different components constituting these systems are still not completely understood. To some extent, the use of geosynthetics as reinforcement preceded the development of suitable methods for analysis and design, and commonly accepted design standards are conservative (Ochiai *et al.* 1993).

The load in the reinforcement and the displacement at the face of reinforced soil walls after construction are usually much smaller than implied by current design methods. For example, even when a wall has been designed to fail (i.e. factor of safety is equal to 1), failure typically occurs at a much higher surcharge load than anticipated based on current design methods (Billiard and Wu 1991). Rimoldi (1988) examined eight cases involving reinforced soil walls and steep slopes using extensible reinforcement, and concluded that the factor of safety against reinforcement rupture was relatively high, suggesting that current design procedures are conservative.

A major issue in reinforced soil wall design is to determine the realistic failure plane. Possible failure due to reinforcement rupture is predicted at the maximum tensile load points. Jewell (1985) stated that the location of maximum tensile load will always be inclined at $45° + \phi/2$ to the horizontal if there is sufficient bond between the fill and the reinforcement, where ϕ is the internal friction angle of backfill. Although there are insufficient data showing the location of the tensile load in different reinforcement lengths, numerical analyses show that the location of the maximum tensile load has a tendency to move towards the facing when the ratio of reinforcement length to wall height is reduced from 0.7 to 0.4 (Jewell 1985).

Several different techniques have been proposed to investigate the actual failure mechanisms in reinforced soil-retaining structures. In these techniques, the investigated system parameters are changed to establish a failure. One of the techniques is the shear strength reduction technique proposed by Matsui and San (1988). In this technique, cohesion (c) and coefficient of friction ($\tan\phi$) are gradually reduced by dividing them by a common shear strength reduction ratio (R). The failure mechanism of a cut slope is examined by using a shear strain failure criterion (strain-based failure judgement method). Accordingly, shear failure occurs when the calculated shear strain exceeds the limit shear strain (i.e. 1%) (Matsui and San 1988). A similar technique was used by San *et al.* (1994), who examined gradually reducing K_0 in subsequent runs from its empirical value ($K_0 = 1 - \sin\phi$) until failure occurred using the strain-based failure judgement method.

Recently a numerical investigation was conducted by Leshchinsky and Vulova (2001) on reinforced soil walls using the finite difference method. They concluded that as the spacing of the reinforcement decreases, the possibility of development of an active failure surface within the reinforced zone decreases. Also, the required reinforcement strength (at working conditions) is nearly half the value rendered by conventional design.

3. NUMERICAL MODEL

The numerical analysis of reinforced soil walls for this parametric study was carried out using the computer program Plaxis. In this finite element program a two-dimensional plane-strain model is used. A geometrical model in this program is a representation consisting of points, lines and clusters. The program automatically recognises clusters based on the input geometry lines. Within the cluster the soil properties are homogeneous (Brinkgreve and Vermeer 1998). In the 2D analyses, the triangular elements have three stress points and six nodes. Displacements are calculated at the nodes, whereas the stresses in each element are calculated at the stress points. The element stiffness matrix is evaluated by numerical (Gaussian) integration using the three stress points.

The analysis was conducted in two phases: the first phase represents the construction process, and the second phase is the determination of the failure conditions of the structure by ϕ–c reduction (Matsui and San 1988). The shear strength parameters, coefficient of friction ($\tan\phi$) and cohesion (c), are incrementally reduced by dividing them by a reduction factor ΣM_{sf} at a given stage in the analysis:

$$\Sigma M_{sf} = \frac{\tan\phi_{input}}{\tan\phi_{reduced}} = \frac{c_{input}}{c_{reduced}} \tag{1}$$

where ϕ_{input} = initial friction angle of the soil, $\phi_{reduced}$ = friction angle of the soil after reduction, c_{input} = initial cohesion of the soil, and $c_{reduced}$ = cohesion of the soil after reduction. The safety factor is then defined as the value of ΣM_{sf}, where for a number of successive incremental reductions the difference between successive ΣM_{sf} becomes very small. The shear strain increments after each calculation step are calculated at every node of the model. Concentrated incremental shear strain zones are considered as the potential failure planes. Evaluating the incremental shear strains at the end of the ϕ–c reduction phase gives a good idea about the failure mechanism despite the fact that the displacement values obtained have no physical meaning (Brinkgreve and Vermeer 1998).

4. MODEL VALIDATION WITH FULL-SCALE TEST DATA

4.1. General

Data from full-scale reinforced soil walls carried out at the Royal Military College of Canada (RMC) (Bathurst *et*

al. 2000) were used for the verification of the results of the current finite element model. Yoo and Song (2006) have also used one of the RMC walls to carry out a similar finite element model verification exercise prior to numerically investigating the influence of foundation yielding on the performance of two-tier segmental retaining walls. Three instrumented full-scale geosynthetic-reinforced test walls (Wall 1, Wall 2 and Wall 3) were modelled using the same finite element code as used in this study. All the walls were 3.6 m high with a target facing batter of 8° to the vertical. They had a maximum 6 m of backfill. The first wall was constructed with 2.52 m long biaxial polypropylene geogrid, and each reinforcement layer had 0.6 m vertical spacing. The second wall was identical to the first one except that the geogrid stiffness and strength was half that of the Wall 1 reinforcement. The third wall had the same geogrid reinforcement and geometry as the first wall, except that the vertical spacing of the geogrids was 0.90 m. All modular facing units were solid masonry blocks with a continuous concrete shear key. The blocks, each weighing 196 N, were 300 mm long, 150 mm high and 200 mm wide. The model dimensions adopted from these full-scale walls are shown in Figure 1. Detailed information about the wall instrumentation and the testing programme is reported by Bathurst *et al.* (2000) and Hatami and Bathurst (2005, 2006).

The mechanical parameters in our finite element model were taken to be the same as the actual full-scale testing data reported by Hatami and Bathurst (2005, 2006). In these references, the actual tests were also verified numerically using a finite difference method. For consistency, most of the parameters used in finite difference analysis input were also employed in the current validation model. Therefore the soil in the validation analysis was modelled by the hardening soil model. In this model the relationship between deviatoric stress and axial strain is approximated by a hyperbola (Figure 2). The hyperbolic

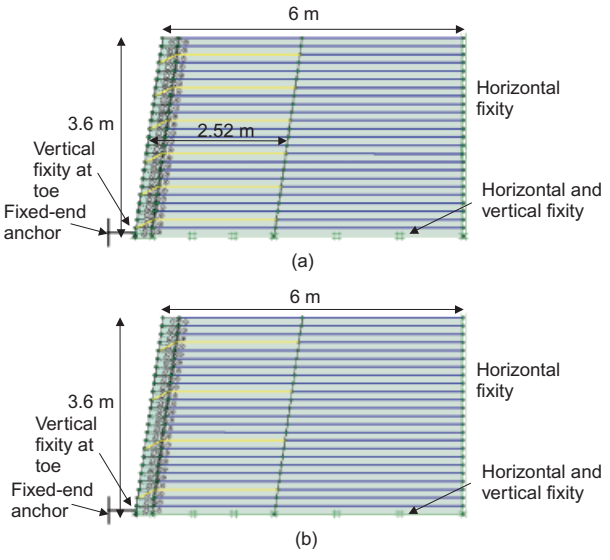

Figure 1. Model geometry and components adopted from full-scale tests: (a) Walls 1 and 2; (b) Wall 3

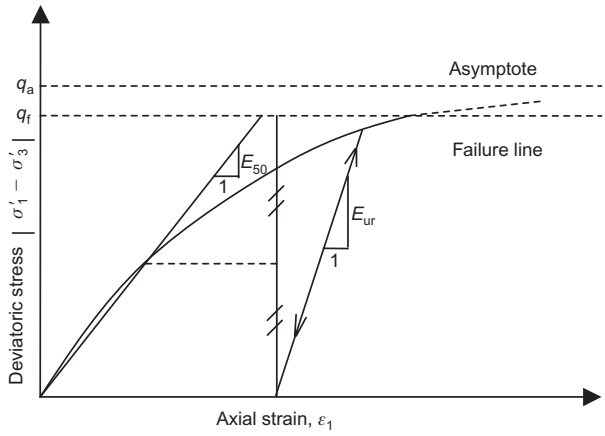

Figure 2. Hyperbolic curve for hardening soil model (from Brinkgreve and Vermeer 1998)

model used here is very similar to the one proposed by Duncan and Chang (1970).

4.2. Soil model and input parameters

The hyperbolic relation between axial strain (ε_1) and deviatoric stress (q) is (Brinkgreve and Vermeer, 1998)

$$\varepsilon_1 = \frac{1}{2E_{50}} \frac{q}{1 - q/q_a} \tag{2}$$

$$q_a = \frac{q_f}{R_f} \tag{3}$$

where q_a is the asymptotic value of the shear strength; q_f is the failure value derived from the Mohr–Coulomb criterion; R_f is the failure ratio, which is taken as 0.9; and E_{50} is the confining stress-dependent stiffness modulus for primary loading, which is given by the equation

$$E_{50} = E_{50}^{ref} \left(\frac{c \cot \phi - \sigma_3'}{c \cot \phi + p^{ref}} \right)^m \tag{4}$$

E_{50}^{ref} is a reference stiffness modulus corresponding to the reference confining pressure p^{ref}, which is usually taken as 100 kPa. The parameters c, ϕ and σ_3' are the cohesion, friction angle and minor principal stress (negative for compression) in a triaxial test, respectively. The amount of stress dependence is given by the power m in the equation. The power m is recommended to be taken close to 0.5 for sands and 1.0 for soft clays (Brinkgreve and Vermeer, 1998). Janbu (1963) reports values of m of about 0.5 for Norwegian sands and silts. Similarly, the value of m for the RMC sand was taken as 0.5.

For loading and unloading stress paths, another stress-dependent stiffness modulus E_{ur} is used, given by

$$E_{ur} = E_{ur}^{ref} \left(\frac{c \cot \phi - \sigma_3'}{c \cot \phi + p^{ref}} \right)^m \tag{4}$$

The finite element software package (Plaxis) uses $E_{ur}^{ref} = 3E_{50}^{ref}$ in the analysis as the default. This value was not changed. A schematic illustration of these parameters is shown in Figure 2.

Hatami and Bathurst (2005) recommend using soil stiffness and strength parameters from plane-strain test

results for numerical analysis rather than triaxial compression test results. Plane-strain compression test results and the estimated hyperbolas at 20 kPa, 30 kPa and 80 kPa normal pressure are shown in Figure 3. It can be seen that there is a good match for confining pressures of 20 kPa and 30 kPa and for strains between 0% and 1.5%. The confining pressure within the 3.6 m high model is not expected to be more than 30 kPa. Also, the axial strain is not expected to be more than 1.5% (Hatami and Bathurst 2005).

The RMC sand friction angle, dilation angle, Poisson's ratio and unit weight are given in Table 1. The cohesion value of 1 kPa was assigned to the backfill soil so that minor local soil failures in the model were prevented. In order to determine the hyperbolic model parameter for the validation model, the plane-strain test results for the RMC sand were employed. As mentioned before, the finite element model uses 100 kPa as the default reference curve for the hyperbolic model. Since no plane-strain compression curve was available for RMC sand at 100 kPa confining pressure, the curve with 80 kPa confining pressure was used as a reference curve. E_{50}^{ref} (at 80 kPa) was back-calculated from Equation 2 and by using the peak strength value of the 80 kPa confining pressure curve ($q_f = 340$ kPa, $\varepsilon_f = 3\%$). The value of R_f was taken as 0.9 to calculate q_a from q_f. After calculating the value of E_{50}^{ref} (at 80 kPa), E_{50} at 20 kPa and 30 kPa can be calculated by using Equation 4. By inputting the calculated E_{50} values at 20 kPa and 30 kPa to Equation 2, the hyperbolas for 20 and 30 kPa confining pressures can be drawn (Figure 3). The calculated parameters are shown in Table 2.

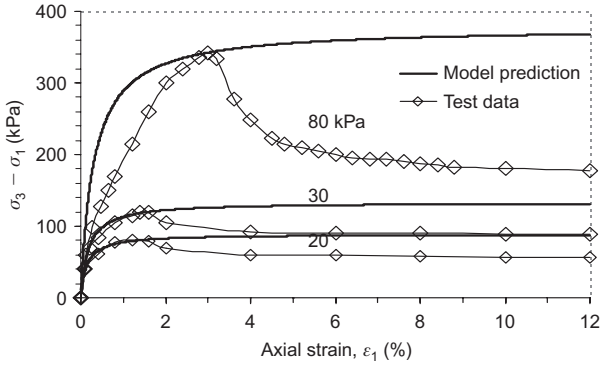

Figure 3. Plane-strain compression tests at different confining pressures and hyperbolic curves (adapted from Hatami and Bathurst 2005)

4.3. Modular blocks and interfaces

Modular blocks are modelled as linear elastic units. Their unit weight, stiffness modulus and Poisson's ratio are given in Table 1. Two different types of interface were utilised: horizontal interfaces between modular blocks, and vertical interfaces between modular blocks and backfill soil. Modular blocks, soil and interfaces are illustrated in Figure 4.

4.4. Geogrid

The extruded biaxial polypropylene geogrid reinforcement was modelled using infinite elastic elements. In the physical models, the geogrid layers are connected to the back of the modular blocks with rigid connectors. In the validation model, geogrids were inserted diagonally into the modular blocks to represent the rigid connection (Figure 4). The bond between elastic modular blocks and

Table 1. Input parameters from full-scale test walls for validation analysis

Soil properties	
Model	Hardening soil model
Soil peak friction angle, ϕ (degrees)	44
Cohesion, c (kPa)	1
Dilation angle, ψ (degrees)	11
Unit weight, γ (kN/m^3)	16.8
Stiffness modulus (kPa)	See Table 2
ν Poisson's ratio	0.25
Modular block properties	
Model	Linear elastic
Unit weight, γ (kN/m^3)	21.8
Stiffness modulus (kPa)	1×10^5
Poisson's ratio, ν	0.15
Block–block horizontal interface	
Block–block friction angle (degrees)	57
Block–block cohesion (kPa)	46
Soil–block vertical interface	
Block–block friction angle (degrees)	44
Soil–block cohesion (kPa)	1
Soil–block dilation angle (degrees)	11
Geogrid	
Elastic axial stiffness (kN/m)	97 (Wall 1 and Wall 3), 48.5 (Wall 2)

Table 2. Hardening soil model parameters used in the model validation analysis

Confining pressure (kPa)	Peak deviatoric stress, q_f (kPa)	Failure ratio, R_f	Asymptotic value of shear strength, q_a (kPa)	Calculated stiffness modulus, E_{50} (kPa)	Stress dependence exponent, m	Stiffness modulus at reference pressure, E_{50}^{ref} (kPa)	Reference pressure, P_{ref} (kPa)
80	340	0.9	378	56 667			
30	120	0.9	133	34 701	0.5	56 667	80
20	80	0.9	89	28 333			

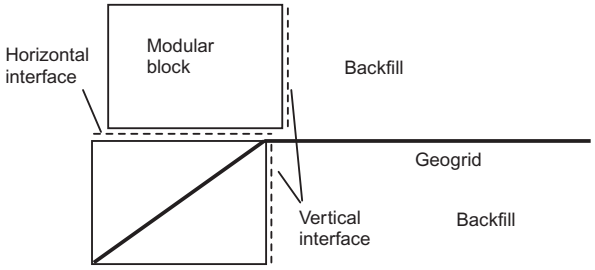

Figure 4. Modular blocks and geogrid connection

the elastic geogrid element was rigid since slippage is not a concern in the elastic model (no shear strength parameter in elastic material). It was observed that there was no evidence of the geogrid pulling out (or deformation) from the modular block after the analysis.

The reinforcement material was represented by a single axial elastic stiffness value. Hatami and Bathurst (2005) suggest taking reduced axial stiffness values that are dependent on axial strain due to creep. Since variable elastic stiffness for the geogrids was not available in the current model, a secant elastic modulus at 1.5% strain was used as an input parameter. A value of 1.5% strain is the maximum strain observed in the geogrids (Hatami and Bathurst 2005). Secant stiffnesses $J_s(\varepsilon)$ for geogrids in Wall 1 and Wall 3 are given by Hatami and Bathurst (2005) as

$$J_s(\varepsilon) = \frac{T(\varepsilon)}{\varepsilon} = 119 - 1469\varepsilon \quad (5)$$

where $T(\varepsilon)$ and ε are the axial load and axial strain, respectively. The secant modulus $J_s(\varepsilon)$ for Wall 2 is half that of Wall 1 and Wall 3. At 1.5% axial strain, the secant modulus for Wall 1, Wall 2 and Wall 3 was calculated as 97 kN/m, 48.5 kN/m and 97 kN/m, respectively.

4.5. Boundary and toe conditions

A horizontal (x-direction) restraint boundary was assigned to the right side of the model, and the bottom boundary of the model was assumed as fixed in both the x and y directions (Figure 1). In the physical model, horizontal steel rollers are located below the toe. These rollers provide a vertical fixity. In order to mimic the roller, a vertical fixity was assumed below the toe in the numerical analysis. Also, a load ring is located on the left side of the footing to provide a horizontal fixity and to enable the measurement of horizontal toe reactions. To simulate the horizontal load ring, a horizontal fixed-end anchor with 4000 kPa axial stiffness was located on the toe, as suggested by Hatami and Bathurst (2005).

4.6. Construction process

The construction of the wall was modelled with the 'staged construction' procedure, where soil layers of 0.15 m thickness (the same as the height of one block) were placed sequentially until the final wall height was reached. A lightweight vibrating plate compactor was simulated by applying an 8 kPa distributed load at every lift using horizontally oriented beam elements. The weight per unit length of the beam elements is taken as 8 (kN/m)/m. The axial stiffness and the flexural rigidity of the beam elements were assigned very small values so that they did not add any strength contribution to the model.

5. VALIDATION OF MODEL RESULTS

5.1. General

All three walls (Wall 1, Wall 2 and Wall 3) were analysed in stages. After placement of each soil layer and the modular blocks, the calculation of that stage was carried out. Reinforcement elements were activated just before placing the upper soil layer. The results of the validation study were evaluated by comparing toe reactions, vertical foundation pressure, horizontal facing displacements and reinforcement strains from the instrumented test walls with values obtained from the finite element model at the end of construction.

5.2. Toe reactions and vertical foundation pressures

The displacements at the toe of the wall were determined during the staged construction phase of the finite element analysis. These displacements were multiplied by the stiffness of the fixed-end anchor to calculate horizontal loads. Vertical toe reactions were taken from total pressure values in each construction step. The average pressure value along the toe is multiplied by the width of the modular block (0.30 m) to find the vertical load below the toe. These reactions were compared with the measured values in Figure 5. From the figure, it can be seen that the calculated horizontal and vertical toe pressures show close agreement with measured values for all three walls.

Vertical foundation pressures below the backfill were obtained from the numerical analysis, and are presented and compared with measured values in Figure 6. The

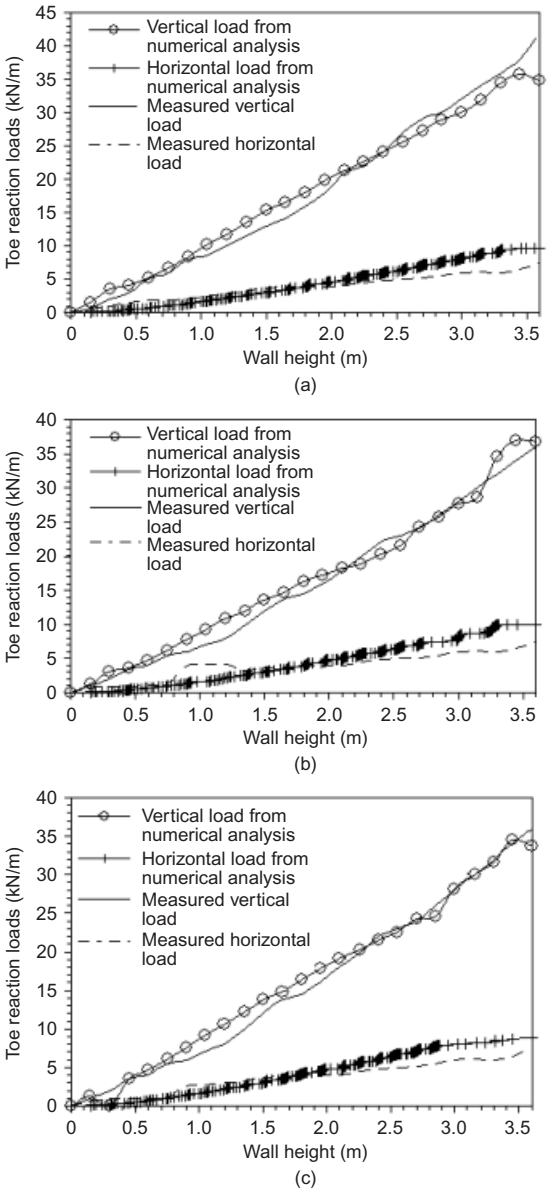

Figure 5. Comparison of vertical and horizontal toe reactions from numerical analysis with measured values reported by Hatami and Bathurst (2005): (a) Wall 1; (b) Wall 2; (c) Wall 3

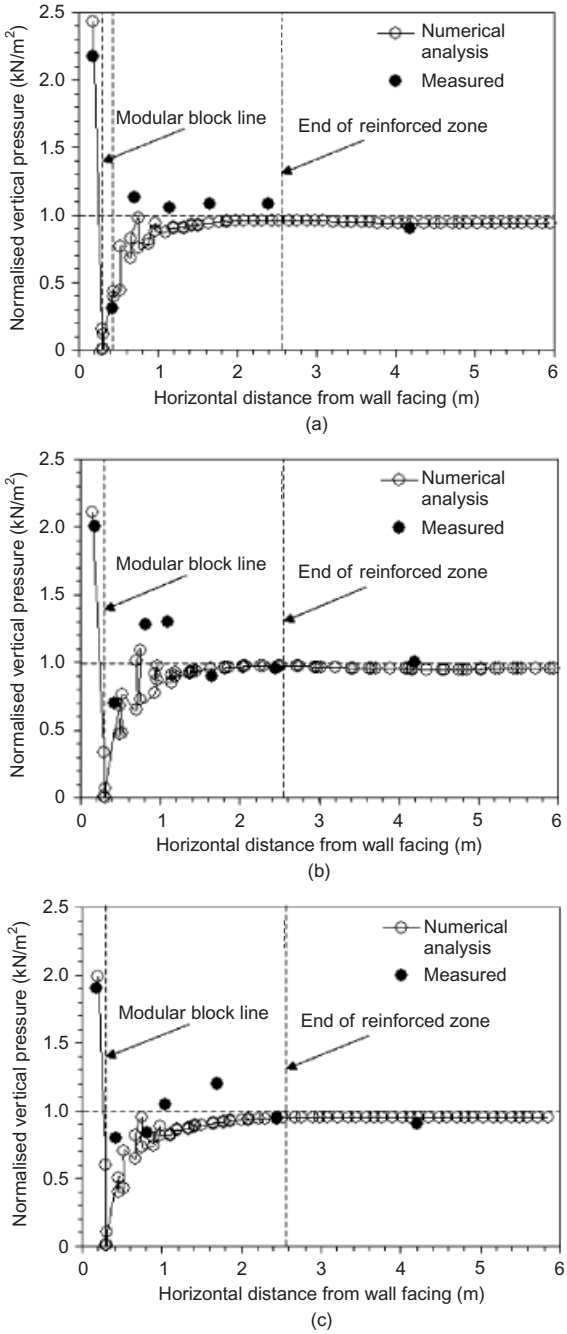

Figure 6. Comparison of normalised foundation pressures obtained from numerical analysis and measured values from Hatami and Bathurst (2005): (a) Wall 1; (b) Wall 2; (c) Wall 3

measured data are presented by normalising the base pressures against the vertical pressure due to soil self-weight (Hatami and Bathurst 2005). The right-hand vertical dotted line indicates the back of the facing column, where measured loads were higher as a result of the greater unit weight of the modular blocks than that of the backfill soil. The measured vertical stresses exhibited a peak behind the modular blocks, whereas the numerical analysis did not. A similar observation was made by Hatami and Bathurst (2005), and they attributed this behaviour to the effect of soil–instrumentation interaction that resulted in a soil arching mechanism between the back of the facing and the rigid foundation base. The values within the reinforced zone are in good agreement with measured values behind the modular blocks and at the end of the reinforced zone and in the unreinforced zone.

5.3. Horizontal facing displacements

The horizontal facing displacements from numerical analysis and measured values from the physical tests are shown in Figure 7. In the numerical analysis, the horizontal facing displacements were determined from the nodes at the facing elements, which are at the same level with the reinforcement. The values correspond to the end of construction phase in the finite element analysis. These values were compared with the measured values taken from the full-scale test models. Hatami and Bathurst (2005) explained that the measured facing displacements were not the actual wall deformation profiles, since the

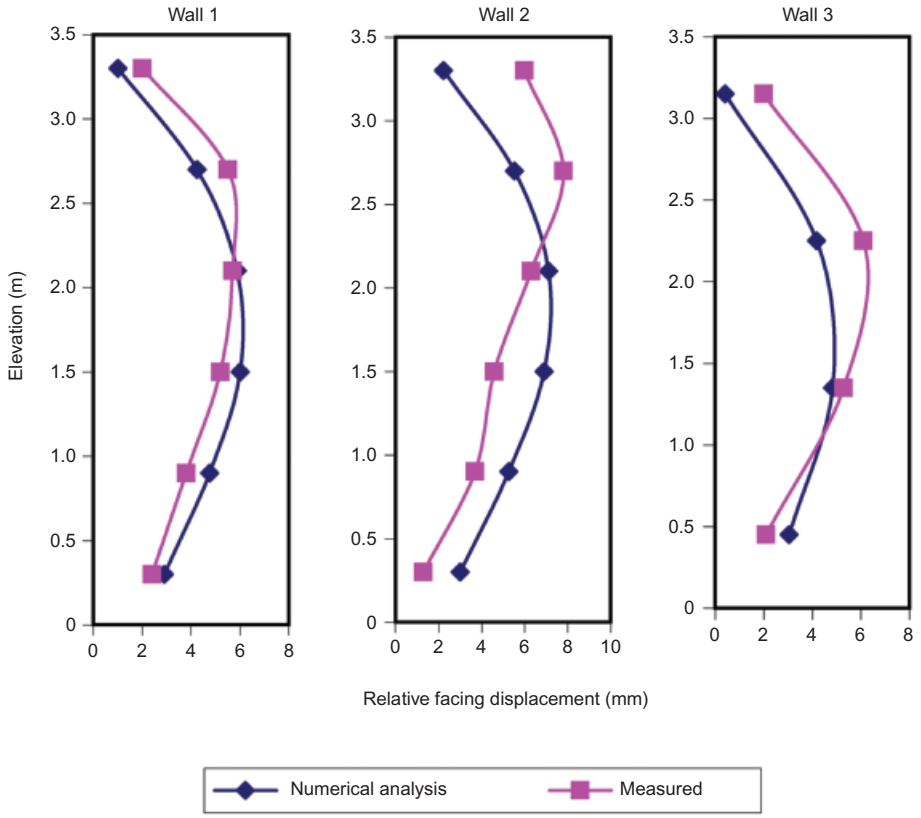

Figure 7. Horizontal facing displacements from numerical analysis and from full-scale test results reported by Hatami and Bathurst (2005)

instrumentation recorded the magnitude of the lateral displacement value from the time of instrument placement to the end of construction. This means that some of the deformation was not recorded. This deformation was most likely so small that there is still a close agreement between the test results and the numerical analysis results for all three walls.

5.4. Reinforcement strains

The axial strains in all reinforcement layers calculated from the finite element analysis at the end of the construction phase were compared with values from full-scale test results. Strains generated in the reinforcement layers of Wall 1 and Wall 2 are shown in Figure 8 and for Wall 3 in Figure 9. Both the extensometer and strain gauge readings are also shown in these plots. Hatami and Bathurst (2005) mention that strain gauges performed better in terms of capturing the reinforcement response at low strain levels (1%). As seen from the figures, strain values obtained from numerical analysis mostly matched the trend in strains obtained from the extensometer and strain gauge readings. For both numerical and measured strains, the peak strain magnitudes close to the connections were captured.

As a general conclusion, the model validation exercise described here shows that the finite element modelling technique used in this research is capable of capturing qualitative trends in the physical model response of full-scale reinforced segmental retaining walls, and in most cases quantitative values are in good agreement as well.

6. FAILURE MECHANISM ANALYSIS

6.1. General

Every component of a reinforced soil-retaining wall has an influence on the wall behaviour. To assess the effects of reinforcement length, vertical reinforcement spacing and backfill type on the failure mechanism, a parametric study was conducted by using the same finite element code described earlier. After analysing the models under working load condition, ultimate failure planes and the factor of safeties were investigated by running a $\phi - c$ reduction analysis.

6.2. Dimensions and boundary conditions

All the models had a wall height (H) of 9 m. The width of the backfill zone was chosen as 25 m. The bottom and side boundaries of the model were located a large distance from the zone of interest (reinforced zone) in order to avoid numerical boundary effects. The lower boundary deformations were fixed in both the horizontal and vertical directions, and the side boundary displacements were fixed only in the horizontal direction. All walls were placed on the stiff foundation, with no boundary restraints assigned. The foundation soil depth was taken as 5 m. Wall facing

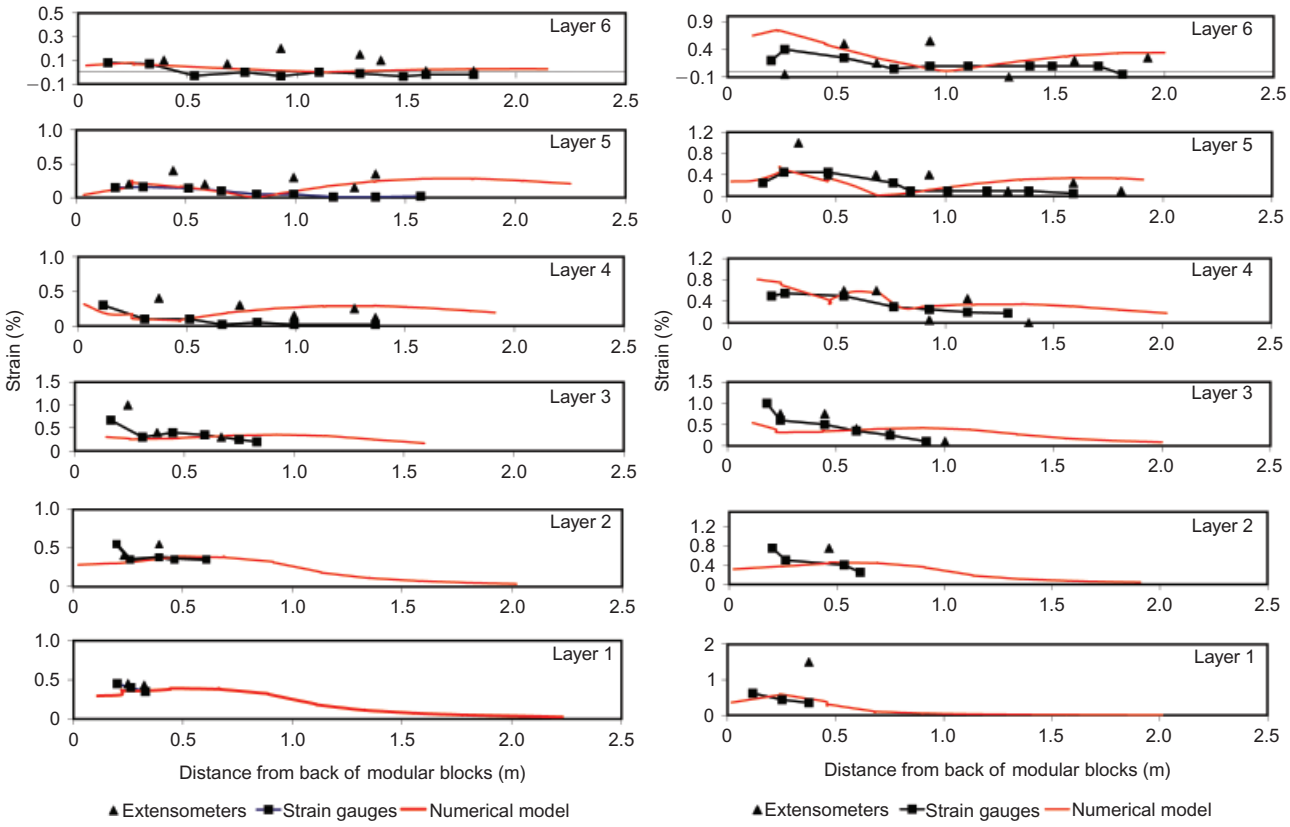

Figure 8. Strain comparisons for Wall 1 and Wall 2 (physical data from Hatami and Bathurst 2005)

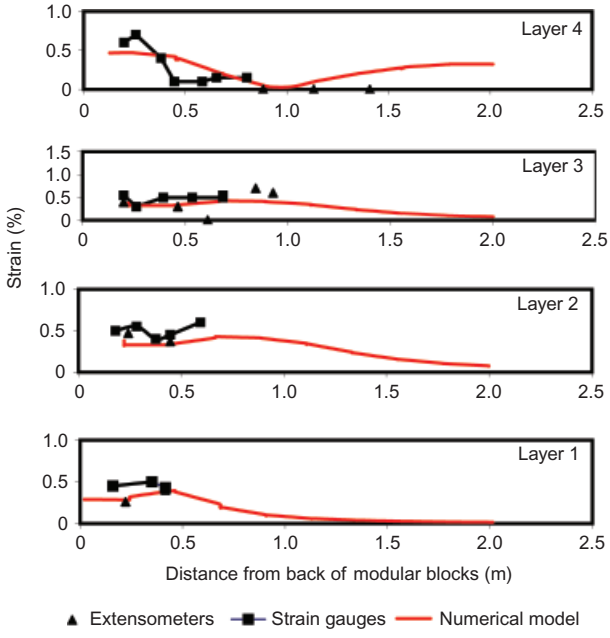

Figure 9. Comparison of strain values from measured data and from numerical model Wall 3 (physical data from Hatami and Bathurst 2005)

elements were constituted with modular block elements. In the 2D model, the modular blocks were modelled with elements of 50 cm width and 25 cm height.

The reinforcement lengths (L) were chosen as 4.5 m, 6 m, 9 m and 13.5 m, which correspond to L/H values of 0.5, 0.67, 1.0 and 1.5, respectively. The spacing of the reinforcement was chosen as either 0.5 m or 1 m. The geometrical dimensions of a typical model (A11) are shown in Figure 10. A total of 16 models with various L/H ratios, reinforcement spacing and backfill type were analysed. The variables used in the finite element analysis are shown in Table 3.

6.3. Material properties

All soil types employed in the model (backfill and foundation soil) and modular blocks were modelled as homogeneous elastic-plastic Mohr–Coulomb materials. Two types of soil were used for the backfill. The first was

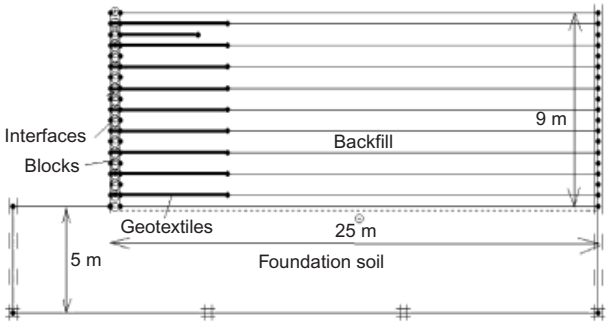

Figure 10. Typical numerical model (model A11)

Table 3. Model combinations used in finite element analysis

Model	Backfill	L/H	ϕ (degrees)	c (kPa)	S_v (m)
A1	Granular	0.50	35	5	0.50
A3		0.67	35	5	0.50
A5		1.00	35	5	0.50
A7		1.50	35	5	0.50
A2	Cohesive	0.50	5	50	0.50
A4		0.67	5	50	0.50
A6		1.00	5	50	0.50
A8		1.50	5	50	0.50
A9	Granular	0.50	35	5	1.00
A11		0.67	35	5	1.00
A13		1.00	35	5	1.00
A15		1.50	35	5	1.00
A10	Cohesive	0.50	5	50	1.00
A12		0.67	5	50	1.00
A14		1.00	5	50	1.00
A16		1.50	5	50	1.00

a granular soil with an internal friction angle of 35° and a cohesion of 5 kN/m^2. The second type was a cohesive soil with cohesion of 50 kN/m^2 and an internal friction angle of 5°. In order not to allow any failure inside the foundation soil, a high cohesion ($c = 200$ kN/m^2) and internal friction angle ($\phi = 35°$) were assigned to the foundation soil. Similarly, a cohesion of 200 kN/m^2 and an internal friction angle of 35° were assigned to the segmental blocks to simulate the modular blocks as a concrete material. The elastic moduli of the backfill soil and foundation soil were taken as 30 000 kN/m^2 and 50 000 kN/m^2, respectively. A higher elasticity modulus of 300 000 kN/m^2 was assigned to the modular facing elements. The soils were modelled as non-dilatant. The dry densities of all soils were taken as 20 kN/m^3.

Reinforcement layers were modelled as tension-only elastic elements, which simulates a woven geotextile. All the reinforcement layers had the same elastic axial stiffness of 1500 kN/m. These elements have no cut-off value against tension. However, the tensile loads in the reinforcement layers were checked that they did not exceed the typical strength values of such materials. The groundwater table was assumed to be deep enough that dry conditions are applicable.

Between each modular block, interface elements were located. The strength properties of the interfaces were linked to the strength properties of the surrounding layer. Each material data value has an associated strength reduction factor (R_{inter}) for the interfaces. The interface properties were calculated from the associated material properties and the strength reduction factor by applying the relations

$$c_i = R_{inter} c_{soil} \quad (6)$$

$$\tan \phi_i = R_{inter} \tan \phi_{soil} \quad (7)$$

where c_i is the cohesion of the interface elements, c_{soil} is the cohesion of the soil that is in contact with the interface, ϕ_i is the friction angle of the interface elements, and ϕ_{soil} is the internal friction angle of the soil. R_{inter} for the block–block interaction was taken as 0.7.

6.4. Stage construction and failure plane determination

In order to simulate wall performance realistically, the first phase of the finite element analysis was the modelling of the construction of the wall. Layers of soils were placed in 0.5 m or 1 m thick layers, depending on reinforcement spacing. The self-weight of each lift was applied incrementally. After the construction phase was complete, a ϕ–c reduction was implemented as the second phase to investigate the ultimate failure plane and safety factor.

7. RESULTS

7.1. Granular backfill

7.1.1. *Effect of reinforcement vertical spacing*

The results of the finite element analysis were evaluated after the stage construction phase, which can be considered as the working condition, and the ϕ–c reduction phase, which can be considered as the failure condition. In models A1 and A9 the reinforcement vertical spacing was 0.5 m and 1.0 m, respectively, and the L/H ratio was 0.5 for both models. The shear strain contours and locations of maximum tensile load points for models A1 and A9 are presented in Figure 11(a) and Figure 11(b), respectively. The shear contour concentrations are denoted as 'Apparent failure line' in these figures. These potential failure planes are linear and partially bilinear, and extend outside the reinforced zone. In these models, it is noted that the locations of shear strain concentration and maximum tensile load points in the reinforcement layers do not coincide exactly. This may be attributed to the insufficient reinforcement length.

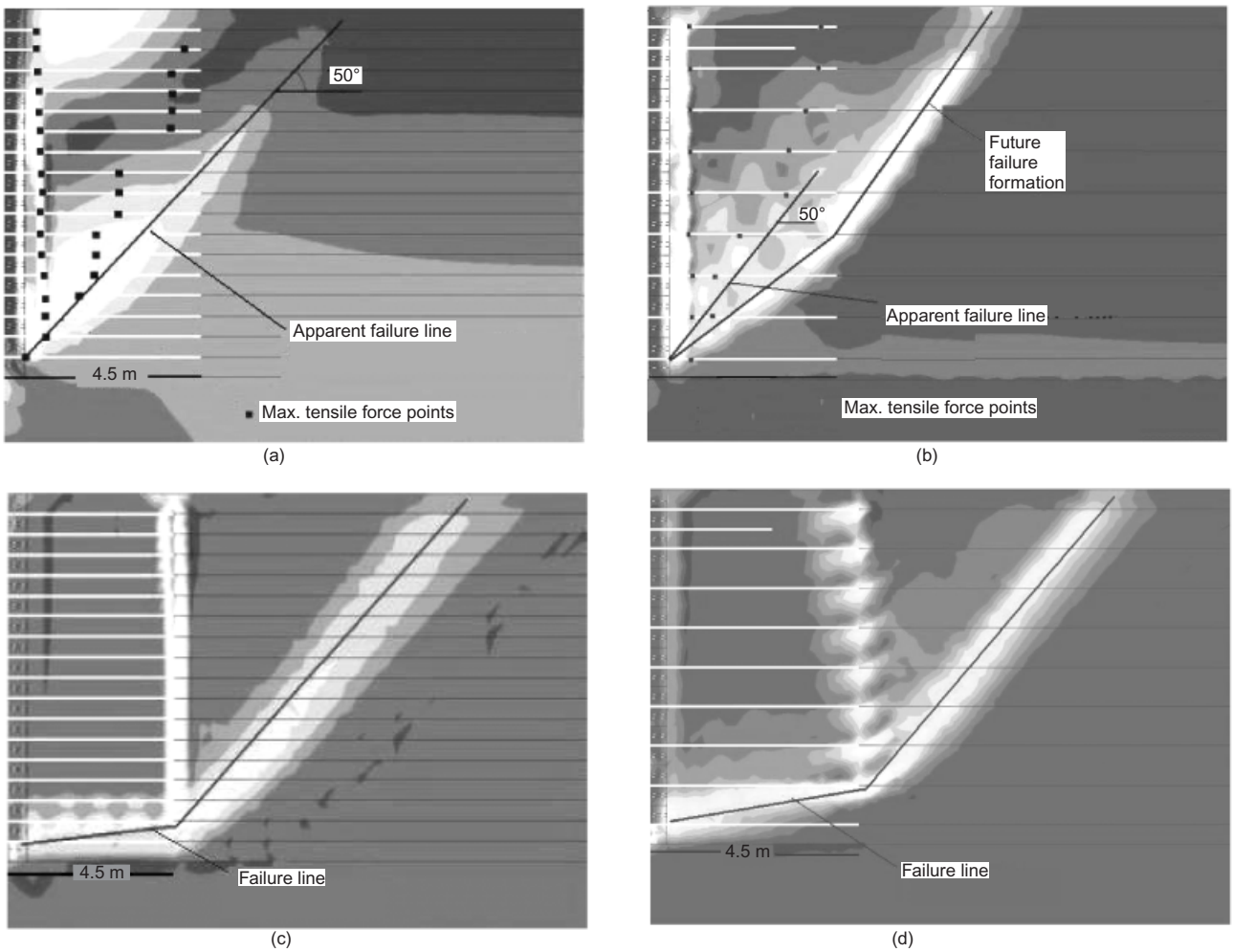

Figure 11. Incremental shear strain contours: (a) at end of construction in model A1 ($L/H = 0.5$ m, $S_v = 0.5$ m); (b) at end of construction in model A9 ($L/H = 0.5$ m, $S_v = 1$ m); (c) at end of ϕ–c reduction in model A1 ($L/H = 0.5$ m, $S_v = 0.5$ m); (d) at end of ϕ–c reduction in model A9 ($L/H = 0.5$ m, $S_v = 1$m)

At the end of ϕ–c reduction, models A1 and A9 show shear concentration patterns (Figures 11c and 11d) that are different from the shear concentration patterns obtained at the end of the construction phase. The shear concentration patterns for vertical reinforcement spacings of 0.5 m and 1 m at the end of ϕ–c reduction are very similar for the two models. The first portion of the bilinear failure plane passes between the lowest two reinforcement layers. The second portion of the shear concentration (failure plane) remains in the unreinforced zone. Model A1, with denser vertical reinforcement spacing, yielded a significantly larger factor of safety value than model A9. The factor of safety values of all the models are given in Table 4. The deformed meshes of models A1 and A9 after ϕ–c reduction analysis are shown in Figure 12. If the deformed meshes of the two models are compared, it can be seen that the reinforced zone of model A1 (0.5 m reinforcement spacing) deforms less than the reinforced zone of model A9 (1 m reinforcement spacing). From Figure 12a (model A1), the reinforced zone translates laterally almost as a monolithic body, and the retained soil shows a deformation that is typical for a Rankine-type failure. This observation indicates that the failure occurs in an external sliding mode. It should be noted that the displacements in these figures are multiplied by a factor of 200 times for clarity. The maximum horizontal wall displacements are all within 10 mm range for all models.

7.1.2. *Effects of reinforcement length*

In order to understand the effect of the reinforcement length on wall response, models A3, A5 and A7 were analysed with a reinforcement vertical spacing of 0.5 m and L/H ratios of 0.67, 1 and 1.5, respectively. Shear strains at the end of construction phase of models A3, A5, and A7 are illustrated in Figure 13. For these models there is good agreement between the location of shear strain concentrations and the maximum tensile load locations in the reinforcement layers. These models have similar shear concentration patterns, and the location of the shear stress concentrations remains completely inside the reinforced zone at the end of the construction. Based on this observation it may be concluded that the locations of shear strain concentration and consequently potential failure planes remain inside the reinforced zone for the models with an L/H ratio of 0.67 or more, at the end of construction. The calculated values of factor of safety indicate that, as the reinforcement length increases, the overall factor of safety value increases significantly (Table 4).

Table 4. Summary of results of finite element analysis

Backfill type	Model no.	L/H	S_v: m	$45° + \phi/2$	Apparent failure line inclination at end of construction (degrees)	Factor of safety
Granular	A1	0.5	0.5	62.5°	50	2.08
	A3	0.67	0.5		56	2.40
	A5	1	0.5		55	3.60
	A7	1.5	0.5		52	–
	A9	0.5	1		50	1.76
	A11	0.67	1		56	2.19
	A13	1	1		60	2.83
	A15	1.5	1		56	3.84
Cohesive	A2	0.5	0.5	47.5°	N/A	2.11
	A4	0.67	0.5		N/A	2.26
	A6	1	0.5		N/A	2.55
	A8	1.5	0.5		N/A	–
	A10	0.5	1		N/A	1.87
	A12	0.67	1		N/A	2.09
	A14	1	1		N/A	2.45
	A16	1.5	1		N/A	–

N/A: Not detected

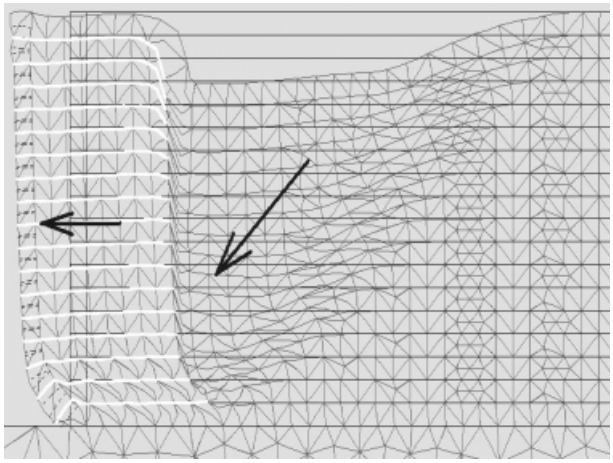

(a)

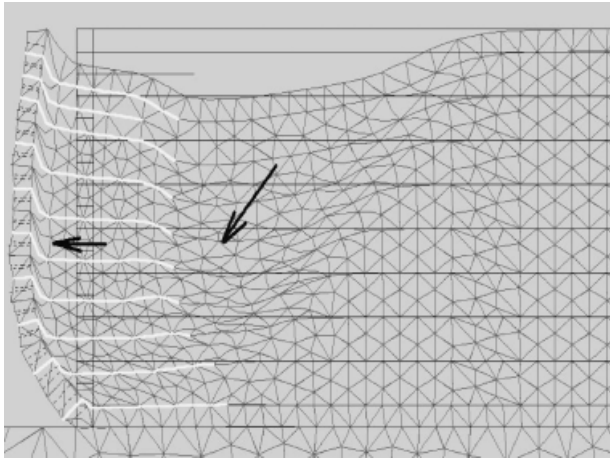

(b)

Figure 12. Deformed mesh at end of $\phi-c$ reduction: (a) in model A1 ($L/H = 0.5$ m, $S_v = 0.5$ m); (b) in model A9 ($L/H = 0.5$ m, $S_v = 1$ m) (displacements scaled by 200 times)

7.1.3. *Failure planes after $\phi-c$ reduction*

The incremental shear strain at the end of $\phi-c$ reduction for model A3 is given in Figure 13d. The location of shear strain concentrations clearly indicates that the failure mechanism is direct sliding. Similar observations can be made for models A5, A7 and A15 (Figures 14a, 14b and 14c, respectively). Figures 13d and 14a indicate that for L/H ratios of 0.67 and 1 there is a tendency for the reinforced zone to separate from the unreinforced zone. This can be determined by the shear strain concentrations directly behind the reinforced zone. This concentration almost disappears for model A7 with an L/H ratio of 1.5 (Figure 14b). Comparison of Figure 14b and 14c further indicates that this is valid only for small vertical reinforcement spacing, since in the model where the vertical spacing of reinforcement was 1 m, the shear strain concentration behind the reinforced zone appears despite the long reinforcement length.

7.1.4. *Transition of shear strain concentration locations*

For granular soils, models A11 and A13 were chosen for further discussion. The shear strain concentrations at the end of the construction phase of models A11 and A13 are illustrated in Figure 14d and 14e, respectively. There are three different zones where the shear strains are concentrated. The first zone seems to appear behind the blocks. The second shear strain concentration zone, which is believed to be the apparent failure surface, appears as a linear line, as shown in Figure 14d. The line makes an angle of approximately 56° with the horizontal. The failure surface mechanism for the walls with extensible reinforcement is assumed to occur with an angle of $45° + \phi/2$ (62.5° for the granular backfill, of this study since $\phi = 35°$), starting from the toe of the wall. Accordingly, the location of the apparent failure line obtained from the

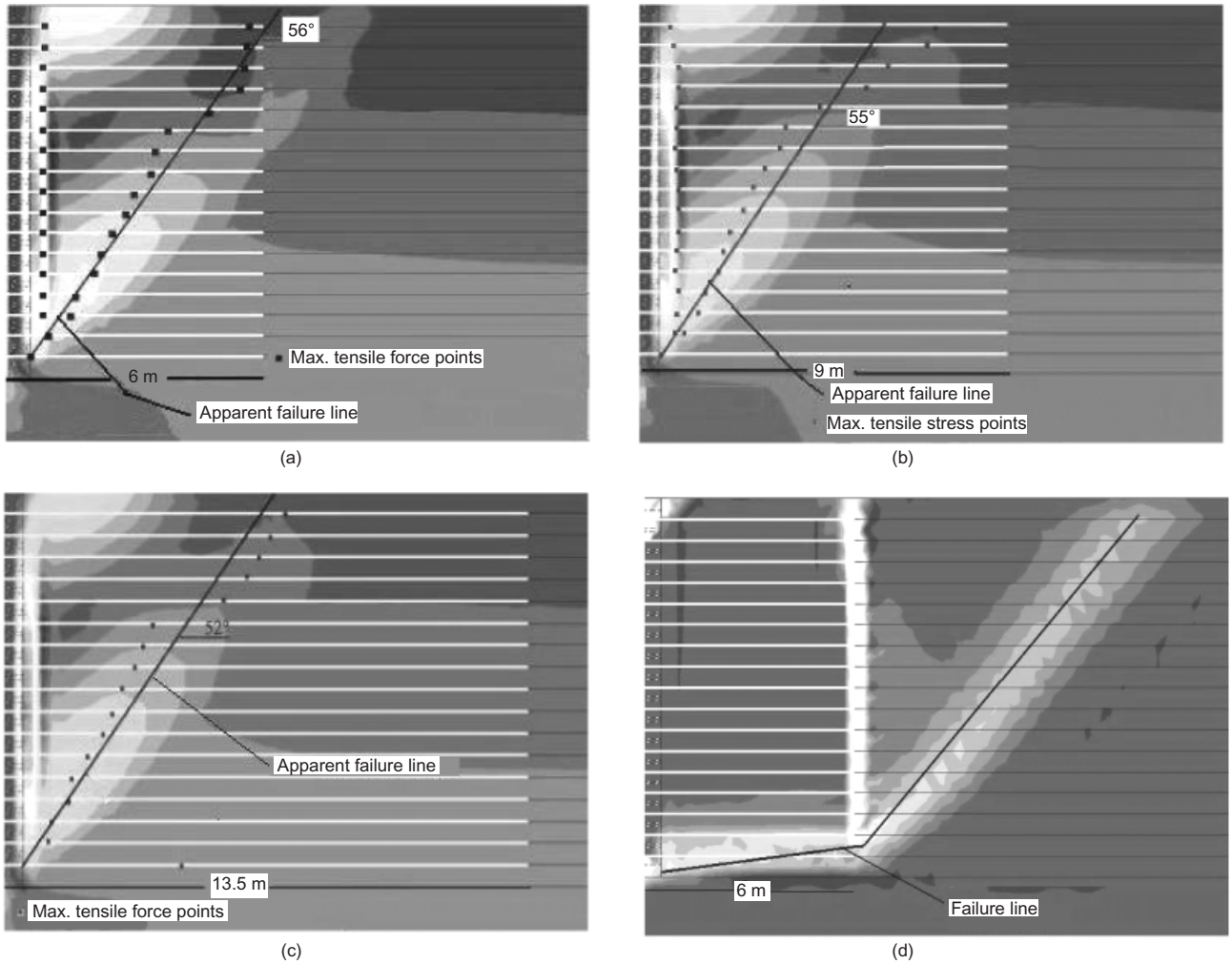

Figure 13. Shear strain contours: (a) at end of construction in model A3 ($L/H = 0.67$ m, $S_v = 0.5$ m); (b) at end of construction in model A5 ($L/H = 1$ m, $S_v = 0.5$ m); (c) at end of construction in model A7 ($L/H = 1.5$ m, $S_v = 0.5$ m); (d) at end of ϕ–c reduction in model A3 ($L/H = 0.67$ m, $S_v = 0.5$ m)

shear strain output data and the failure surface assumed in conventional design appear to be reasonably close. It can be seen that a third bilinear shear strain concentration zone formed just below the apparent failure line, which is denoted as 'Formation of ultimate failure' in Figure 14d. In model A13, since the reinforcement lengths are longer, this additional shear strain concentration along a bilinear surface has not yet developed at the end of construction (Figure 14e).

All the incremental shear strains between the end of construction phase the ϕ–c reduction phase were successively put together for model A11 by an animation technique to monitor the change of location of the incremental shear strain concentrations. As the ϕ and c values were gradually decreased, the 'Apparent failure line' shown in Figure 14d gradually disappeared and the bilinear shear strain concentration line denoted as the 'Formation of ultimate failure' line moved downwards, changing to the bilinear failure plane given in Figure 14f. From the deformed mesh given in Figure 15 it can be seen that the reinforced zone has drifted to the left, and a failure wedge has developed in the unreinforced zone. Excessive plastic deformations occur within the lowest layer of the reinforced zone, and the remaining upper reinforced body has drifted almost in an undeformed shape. When this mechanism and the gradual drift of the potential failure surface are considered together, it can be stated that the internal failure mechanism within the reinforced zone is not critical, and if the reinforced soil system fails, it will fail in the direct sliding mode.

7.1.5. *Tensile loads in reinforcement*

Tensile loads in the reinforcement layers at the end of the construction phase are in the range 5 to 15 kN/m. As an example, all maximum tensile loads calculated for model A11 are given in Table 5. Breakage of reinforcement is not expected, because these tensile loads can be safely carried by most reinforcement geosynthetics. A limit equilibrium calculation shows that the maximum tensile load for similar geometry and soil conditions reaches values above 25 kN/m. Maximum tensile load locations in the reinforcement layers are marked in Figure 14e by black squares. From this figure it can be seen that there were two locations where the tensile loads have peak values. The maxima on the left side always stay within the zone of the shear strain concentration behind the blocks,

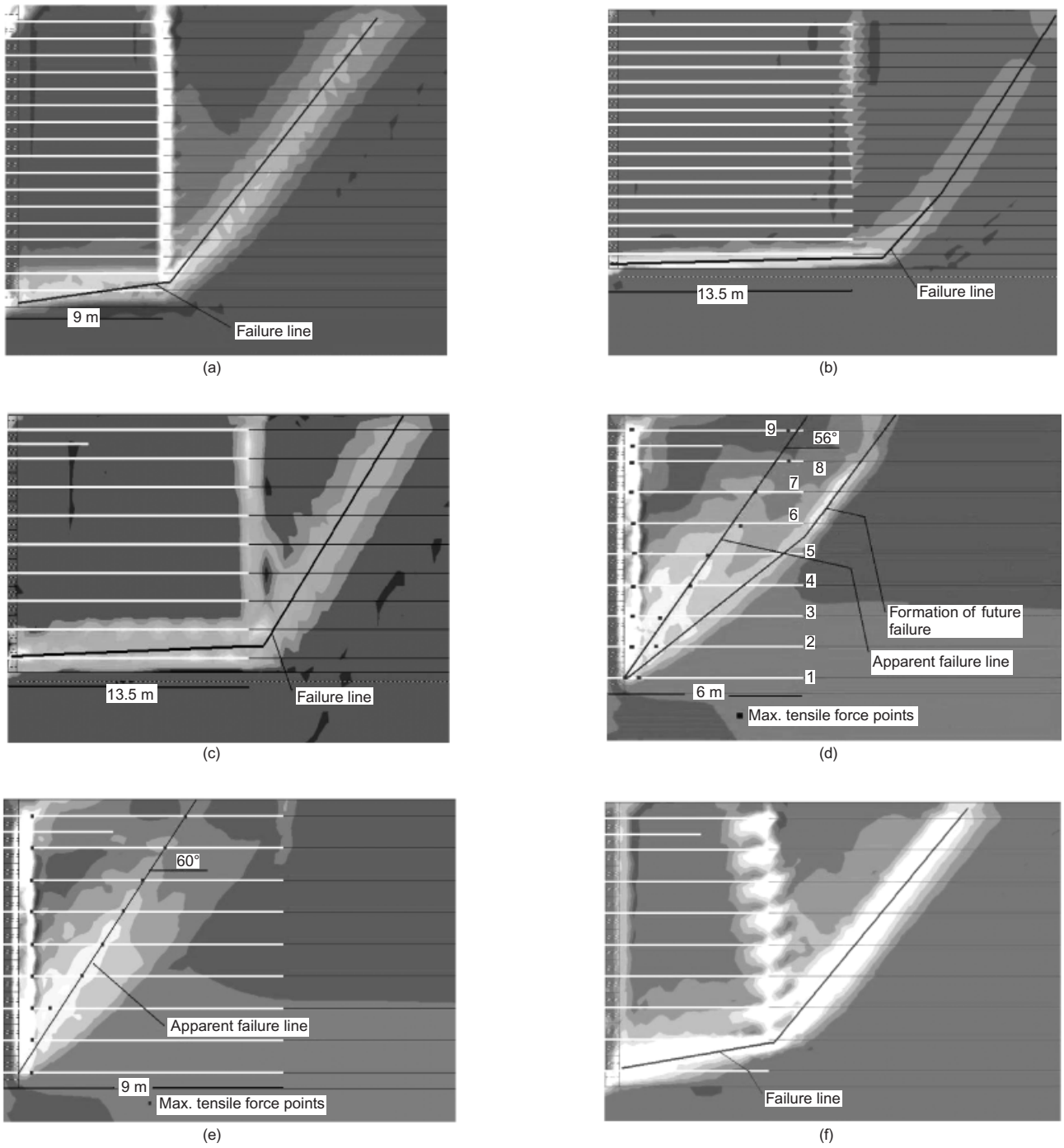

Figure 14. Incremental shear strain contours: (a) at end of ϕ–c reduction in model A5 ($L/H = 1$ m, $S_v = 0.5$ m); (b) at end of ϕ–c reduction in model A7 ($L/H = 1.5$ m, $S_v = 0.5$ m); (c) at end of ϕ–c reduction in model A15 ($L/H = 1.5$ m, $S_v = 1$ m); (d) at end of construction in model A11 ($L/H = 0.67$ m, $S_v = 1$ m); (e) at end of construction in model A13 ($L/H = 1$ m, $S_v = 1$ m); (f) at end of ϕ–c reduction in model A11 ($L/H = 0.67$ m, $S_v = 1$ m)

and the maxima on the right side are very close to the apparent failure line. A typical tensile load distribution plot is illustrated in Figure 16.

7.2. Cohesive backfill

Models with cohesive backfill behave similarly, regardless of reinforcement length or reinforcement spacing. Model A12 was chosen to represent the behaviour of models with cohesive backfill, and the shear strains at the end of construction phase are illustrated in Figure 17a in the form of shear strain contours. Unlike granular backfills, there was no definitive shear strain concentration zone forming at the end of the construction phase. In ϕ–c reduction analysis of the same model it was observed that the incremental shear strains concentrate along a bilinear zone (Figure 17b). This behaviour was similar to that obtained for models with granular backfills. This observation indicates that for cohesive backfills also the critical failure mode is external sliding. Although walls with granular and cohesive backfills showed different behaviour in terms

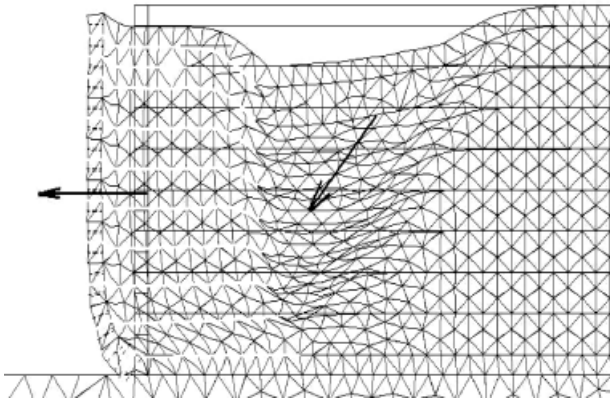

Figure 15. Deformed mesh at end of $\phi-c$ reduction in model A11 ($L/H = 0.67$ m, $S_v = 1$ m) (displacements multiplied 200 times)

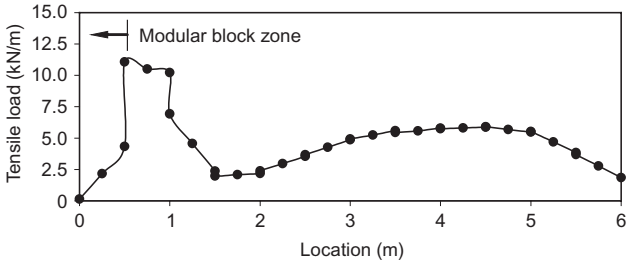

Figure 16. Tensile loads in reinforcement layer 7 in model A11

of potential failure planes at the end of the construction phase, similar behaviour was observed at the end of $\phi-c$ reduction (failure condition). Locations of the incremental shear contour concentrations indicate that the failure mechanism of walls with cohesive backfill is almost the same as that of walls with granular backfill.

The calculated tensile loads in the reinforcement layers with cohesive backfill soils were lower than the tensile loads in reinforcement layers in granular backfill. They ranged between 1 and 3 kN/m. The maximum horizontal displacement for model 12 was 7 mm. This deformation was similar to the horizontal displacement obtained for model A11, which had the same reinforcement configuration as Model 12 except for the backfill type. Also, for cohesive backfill, higher factor of safety values were obtained for longer reinforcement layers and closer reinforcement spacing (Table 4).

8. CONCLUSIONS AND DISCUSSION

A parametric study was conducted to examine predicted failure mechanisms of reinforced soil walls using finite element analysis. First, a validation study of the numerical model was conducted by comparing the results obtained from well-instrumented full-scale reinforced soil wall tests reported by Hatami and Bathurst (2005) with the results of the finite element analysis of the same structures. The results of the validation study indicated that the horizontal wall facing displacements, and toe and foundation reactions of the test walls were in reasonable agreement with numerical predictions. Strain values measured in the reinforcements were of the same order of magnitude and had similar trends as the numerical analysis results.

For geosynthetic-reinforced walls with granular backfill, the finite element analyses results showed that the locations of shear strain concentration at the end of the construction phase were in good agreement with the failure planes currently assumed in limit equilibrium analysis methods. This shows that the potential failure surfaces used in current limit equilibrium-based design methods (e.g. FHWA, 1997; NCMA 1997) to analyse the factors of safety of geosynthetic-reinforced soil-retaining structures are correct.

Shear strains obtained from the finite element analyses indicated that when the design loads are exceeded (or the system is no longer safe), the direct sliding mode becomes the controlling failure mode for wall with both granular and cohesive soils, if the geosynthetic-reinforced retaining structure is constructed on a firm foundation. As the ratio of reinforcement length to height increased, the separation between the reinforced and retained soil decreased. It was also observed that the vertical reinforcement spacing has an effect on this behaviour. For a reinforcement spacing of 0.5 m, it was observed that, even when the system as a whole approaches failure, the reinforced zone remains almost intact. For reinforcement spacing of 1 m, larger deformations in the reinforced zone were observed. Re-

Table 5. Tensile loads in reinforcement layers of model A11

Reinforcement no.[a]	Load[b] (kN)	Distance from facing (m)	Load[c] (kN)
9	4.0	5.5	2.8
8	5.9	5.5	2.8
7	10.5	4.5	5.9
6	12.1	4	7.63
5	12.7	2.5	9
4	13.2	2.5	10.2
3	13.4	1.5	10.7
2	8.9	1.5	7.9
1	3.5	1	7

[a]Locations of reinforcement layers are shown in Figure 14d.
[b]Peak tensile load immediately behind the blocks.
[c]Peak tensile load in the remaining length.

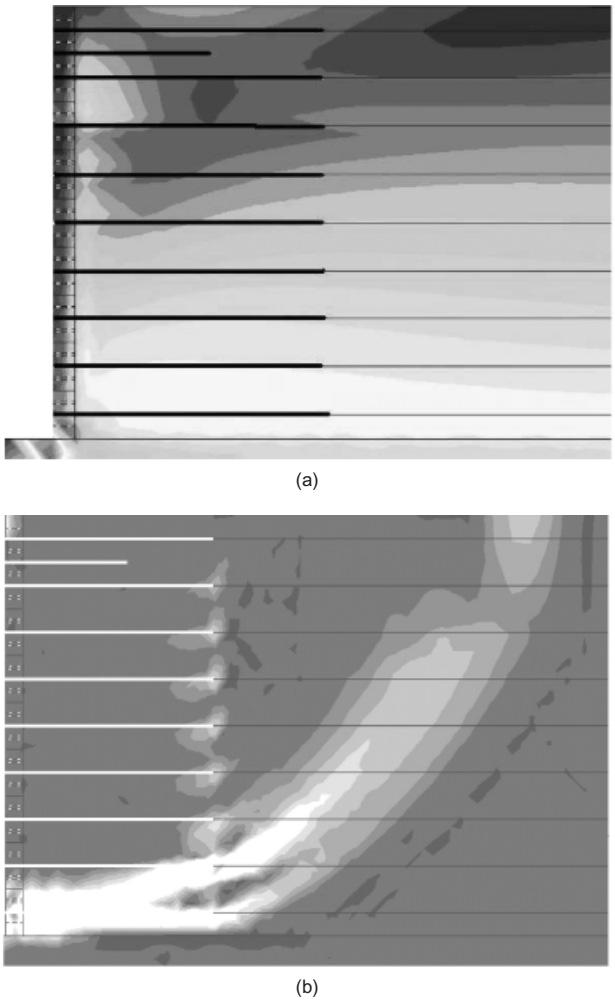

Figure 17. Shear strain contours: (a) at end of construction in model A12 ($L/H = 0.67$ m, $S_v = 1$ m); (b) at end of ϕ–c reduction in model A12 ($L/H = 0.67$ m, $S_v = 1$ m)

inforcement layers developed high loads and strains just behind the facings because of the rotation of the facing and differential vertical settlement between the reinforced soil and the rigid facing elements.

For walls with cohesive backfill, the tensile loads in the reinforcement were lower than for walls with granular backfills. Additionally, for cohesive backfill, no shear strain concentrations were obtained in the finite element analysis at the end of construction, which indicates that no internal failure mechanism developed under working load conditions for the geometry and reinforcement configurations investigated. Both cohesive and granular soils seemed to be adequate backfill materials for the modelled cases. In practice, this can only be ensured if proper drainage measures are provided.

NOTATIONS

Basic SI units are given in parentheses.

c	cohesion (Pa)
c_i	interface cohesion (Pa)
c_{input}	initial cohesion of soil (Pa)
$c_{reduced}$	cohesion of soil after reduction (Pa)
E	elastic modulus (Pa)
EA	elastic axial stiffness (N/m)
E_{50}	confining stress-dependent stiffness modulus for primary loading (Pa)
E_{50}^{ref}	reference stiffness modulus corresponding to reference confining pressure p^{ref} (Pa)
E_{ur}^{ref}	unloading and reloading stress-dependent stiffness modulus (Pa)
H	wall height (m)
K_a	horizontal active earth pressure coefficient (dimensionless)
K_0	horizontal at rest earth pressure coefficient (dimensionless)
L	reinforcement length (m)
m	stress dependence exponent (dimensionless)
p^{ref}	reference confining pressure (= 100 kPa)
q_a	asymptotic value of shear strength (Pa)
q_f	failure value derived from Mohr–Coulomb criterion (Pa)
R_f	failure ratio (dimensionless)
R_{inter}	strength reduction factor for interfaces (dimensionless)
S_v	reinforcement vertical spacing (m)
γ	unit weight of soil (N/m^3)
ε_1	axial strain (dimensionless)
ε_f	axial strain at peak deviatoric stress (dimensionless)
μ	coefficient of friction (dimensionless)
ν	Poisson's ratio (dimensionless)
ϕ_i	interface friction angle (degrees)
ϕ_{input}	initial friction angle of soil (degrees)
$\phi_{reduced}$	reduced friction angle of soil (degrees)
ϕ_{soil}	internal friction angle (degrees)
ψ	dilation angle of soil (degrees)
ΣM_{sf}	reduction factor used in finite element ϕ–c reduction analysis (dimensionless)

REFERENCES

Bathurst, R. J., Walters, D., Vlachopoulos, N., Burgess, P. & Allen, T. M. (2000). Full scale testing of geosynthetic reinforced walls: Invited Keynote Paper. ASCE Special Publication No. 103, *Advances in Transportation and Geoenvironmental Systems using Geosynthetics, Proceedings of Geo-Denver 2000*, August 2000, Denver, CO, USA, pp. 201–217.

Benjamim, C. V. S., Bueno, B. S. & Zornberg, J. G. (2007). Field monitoring evaluation of geotextile-reinforced soil-retaining walls. *Geosynthetics International*, **14**, No. 2, 100–118.

Billiard, J. W. & Wu, J. T. H. (1991). Load test of a large-scale geotextile-reinforced retaining wall. *Proceedings of Geosynthetic '91 Conference*, New Orleans, USA, Vol. 2, pp. 537–548.

Brinkgreve, R. B. J. & Vermeer, P. A. (1998). *Finite Element Code for Soil and Rock Analyses*, Version 7.2, Balkema, Rotterdam.

Duncan, J. M. & Chang, C.-Y. (1970). Nonlinear analysis of stress and strain in soil. *Journal of the Soil Mechanics and Foundations Division, ASCE*, **96**, No. 5, 1629–1653.

Elias, V. & Christopher, B. R. (1997). Mechanically stabilized earth walls and reinforced soil slopes: Design and construction guidelines. *Federal Highway Administration Demonstration Project 82 Reinforced Soil Structures*, National Technical Information Service, Springfield.

FHWA (1997). *Mechanically Stabilized Earth Walls and*

Reinforced Slopes: Design and Construction Guidelines, Report Number FHWA-SA-96-071. Federal Highway Administration, Washington, DC.

Hatami, K. & Bathurst, R. J. (2005). Development and verification of a numerical model for the analysis of geosynthetic-reinforced soil segmental walls under working stress conditions. *Canadian Geotechnical Journal*, **42**, No. 4, 1066–1085.

Hatami, K. & Bathurst, R. J. (2006). A numerical model for reinforced soil segmental walls under surcharge loading. *ASCE Journal of Geotechnical and Geoenvironmental Engineering*, **132**, No. 6, 673–684.

Janbu, J. (1963). Soil compressibility as determined by oedometer and triaxial tests. *Proceedings of the European Conference on Soil Mechanics and Foundation Engineering*, Wiesbaden, Vol. 1, pp. 19–25

Jewell, R. A. (1985). Limit equilibrium analysis of reinforced soil walls. *Proceedings of the 11th International Conference on Soil Mechanics and Foundation Engineering*. Balkema, Rotterdam, The Netherlands, pp. 1705–1708.

Leshchinsky, D. & Vulova, C. (2001). Numerical investigation of the effects of geosynthetic spacing on failure mechanisms in mechanically stabilized earth block walls. *Geosynthetics International,* **8**, No. 4, 343–365.

Matsui, T. & San, K. C. (1988). Finite element stability analysis method for reinforced slope cutting. *International Geotechnical Symposium on Theory and Practice of Earth Reinforcement*, Fukuoka, Japan, pp. 317–322.

NCMA (1997). *Design Manual for Segmental Retaining Walls*, 2nd edn, Collin, J. G. (Editor). National Concrete Masonry Association, Herndon, VA, USA.

Ochiai, H., Hayashi, S. & Otani, J. (1993). Earth reinforcement practice. *Proceedings of the International Symposium on Earth Reinforcement Practice*, Fukuoka, Kyushu, Japan, 11–13 November 1992, Vol. 2, pp. 801–828.

Rimoldi, P. (1988). A review of field measurements of the behavior of geogrid reinforced slopes and walls. *Proceedings of the International Geotechnical Symposium on Theory and Practice of Earth Reinforcement*, Fukuoka, Japan, 5–7 October, pp. 571–578.

San, K., Leshchinsky, D. & Matsui, T. (1994). Geosynthetic reinforced slopes: limit equilibrium and finite element analyses. *Soils and Foundations*, **34**, No. 2, 79–85.

Yoo, S. & Song, A. R. (2006). Effect of foundation yielding on performance of two-tier geosynthetic-reinforced segmental retaining walls: a numerical investigation. *Geosynthetics International*, **13**, No. 5, 181–194.

Zornberg, J. G. & Mitchell, J. K. (1994). Reinforced soil structures with poorly draining backfills. Part I: Reinforcement interactions and functions. *Geosynthetics International*, **1**, No. 2, 103–147.

The Editor welcomes discussion on all papers published in Geosynthetics International. Please email your contribution to discussion@geosynthetics-international.com by 15 June 2008.